Supporting Information

Supporting Information Corrected May 16, 2013
Sun et al. 10.1073/pnas.1220610110

SI Discussion

Detailed Implications of the Importin-α Mutant Results. Fig. S5 illustrates the interactions of the three importin-α (Imp-α) mutations discussed in this paper. Critical to understanding these mutations is the fact that Imp-α contains two nuclear localization signal (NLS) binding sites, termed major and minor NLS binding sites. Relevant properties of the Imp-α mutations are as follows.

D192K. The D192K mutation is located in the major NLS binding site (Fig. S5*A*) (1, 2). The simian virus 40 (SV40) NLS, which is found in the NLS-2xGFP cargo, binds to the major NLS binding site (3). As expected, the D192K Imp-α mutant exhibits a substantially lower affinity for the NLS-2xGFP cargo (Fig. S2*A*).

E396R. The E396R mutation is located in the minor NLS binding site (Fig. S5*B*) (4, 5). The E396R mutant has a slightly reduced affinity (less than twofold) for the NLS-2xGFP cargo (Fig. S2*A*), consistent with the fact that the SV40 NLS on the NLS-2xGFP cargo binds primarily, but not exclusively, to the major NLS binding site (3). More importantly, nucleoporin (Nup)50 binds to two locations on Imp-α. The Imp-α binding site for Nup50 residues 1–15 (binding segment 1) overlaps the minor NLS binding site (Fig. S5*B*), whereas the binding site for Nup50 residues 24–46 (binding segment 2) overlaps the CAS/RanGTP interaction site (5). As expected, the E396R mutant has a significantly reduced affinity for Nup50 (Fig. S2*D*).

R39D. The importin-β (Imp-β) binding (IBB) domain autoinhibits NLS binding by simultaneously binding to both major and minor NLS binding sites (4). The R39D mutation is located in the IBB domain between the two NLS binding-site segments (Fig. S5*C*). The R39D mutant has a reduced affinity for CAS (Fig. S2*B*), as expected due to the interaction of Imp-α Arg39 with CAS Asp226 (4).

With this background, we now provide a more expanded analysis of the single-molecule fluorescence resonance energy transfer (smFRET) results.

The D192K mutation reduced Imp-α/CAS complex formation by approximately twofold (Fig. 4). The CAS and NLS binding regions are well separated on Imp-α (4), so no direct influence of the D192K mutation on binding of Imp-α to CAS was expected. However, the Imp-α IBB domain autoinhibits NLS binding (6), and, in doing so, Lys49 of the IBB domain interacts with Asp192, an interaction that is expected to be substantially weakened in the D192K mutant. Moreover, structural studies of the yeast CAS homolog, Cse1, have suggested that formation of the Cse1/RanGTP/Imp-α export complex is promoted by binding of the Imp-α IBB domain to the major and minor NLS binding sites on Imp-α (4). These structural data and our smFRET data suggest that kinetically efficient binding of CAS/RanGTP to Imp-α requires an NLS or IBB domain bound at the major NLS binding site. Imp-α(D192K)/CAS complexes that did form during nuclear import never dissociated at the nuclear pore complex (NPC) (Fig. 4). Thus, although formation of the Imp-α(D192K)/CAS interaction was kinetically inefficient, this interaction was stable once formed. The affinity of the D192K mutant for cargo is so weak (Fig. S2*A*) that none of the cargo-containing species in Fig. 4 are expected to form. Consequently, there is no trimeric cargo/Imp-α/CAS intermediate for this mutant and so one decay pathway (pathway 5 in Fig. 4) is simply unavailable.

The E396R mutation reduced Imp-α/CAS complex formation by approximately fivefold (Fig. 4). Because this mutation substantially reduces the affinity of Imp-α for Nup50 (Fig. S2*D*), these data support the hypothesis that Imp-α/cargo complex disassembly and Imp-α/CAS complex formation are choreographed by Nup50, consistent with in vitro data (5, 7–10).

The R39D mutation reduced Imp-α/CAS complex formation by ∼10-fold (Fig. 4). This is explained by the interaction of Imp-α Arg39 with CAS Asp226, as described above. However, Arg39 also is important for other interactions. R39D is in the IBB domain of Imp-α, which directly interfaces as an α-helix with Imp-β (11). Thus, the affinity of Imp-β for Imp-α is expected to be substantially weakened by the R39D mutation. Thus, the autoinhibited form of the R39D mutant of Imp-α is expected to dominate, even in the presence of Imp-β (6), explaining why Imp-α(R39D) has a reduced affinity for cargo (Fig. S2*A*). Consequently, as for the D192K mutant, it is possible that none of the various species in Fig. 4 contain the cargo for the R39D mutant. However, it is unclear how autoinhibited Imp-α (free of cargo and Imp-β) could interact with NPCs, as we did not observe such interactions in single-molecule experiments with wild-type Imp-α in the absence of Imp-β.

The transient cargo/Imp-α/CAS/RanGTP/Nup50 complex postulated in Fig. 6 requires numerous simultaneous interactions of other proteins with Imp-α. Although binding segment 2 of Nup50 and CAS/RanGTP cannot bind simultaneously to Imp-α, the interaction of Nup50 binding segment 1 with Imp-α is sufficient to explain the association of Imp-α with CAS/RanGTP observed in our smFRET experiments. Thus, the interaction of Imp-α with Nup50, at least initially, is likely to involve primarily binding segment 1 alone. Moreover, we expect that in the transient cargo/Imp-α/CAS/RanGTP/Nup50 complex, the cargo is bound via its NLS in the major NLS binding site, Nup50 binding segment 1 interacts with the minor NLS binding site, and CAS/RanGTP interacts with a region of Imp-α that overlaps with Nup50 binding segment 2.

1. Gruss OJ, et al. (2001) Ran induces spindle assembly by reversing the inhibitory effect of importin alpha on TPX2 activity. *Cell* 104(1):83–93.
2. Giesecke A, Stewart M (2010) Novel binding of the mitotic regulator TPX2 (target protein for Xenopus kinesin-like protein 2) to importin-α. *J Biol Chem* 285(23):17628–17635.
3. Kobe B (1999) Autoinhibition by an internal nuclear localization signal revealed by the crystal structure of mammalian importin alpha. *Nat Struct Biol* 6(4):388–397.
4. Matsuura Y, Stewart M (2004) Structural basis for the assembly of a nuclear export complex. *Nature* 432(7019):872–877.
5. Matsuura Y, Stewart M (2005) Nup50/Npap60 function in nuclear protein import complex disassembly and importin recycling. *EMBO J* 24(21):3681–3689.
6. Catimel B, et al. (2001) Biophysical characterization of interactions involving importin-α during nuclear import. *J Biol Chem* 276(36):34189–34198.
7. Gilchrist D, Mykytka B, Rexach M (2002) Accelerating the rate of disassembly of karyopherin.cargo complexes. *J Biol Chem* 277(20):18161–18172.
8. Gilchrist D, Rexach M (2003) Molecular basis for the rapid dissociation of nuclear localization signals from karyopherin alpha in the nucleoplasm. *J Biol Chem* 278(51): 51937–51949.
9. Matsuura Y, Lange A, Harreman MT, Corbett AH, Stewart M (2003) Structural basis for Nup2p function in cargo release and karyopherin recycling in nuclear import. *EMBO J* 22(20):5358–5369.
10. Solsbacher J, Maurer P, Vogel F, Schlenstedt G (2000) Nup2p, a yeast nucleoporin, functions in bidirectional transport of importin alpha. *Mol Cell Biol* 20(22):8468–8479.
11. Cingolani G, Petosa C, Weis K, Müller CW (1999) Structure of importin-β bound to the IBB domain of importin-alpha. *Nature* 399(6733):221–229.

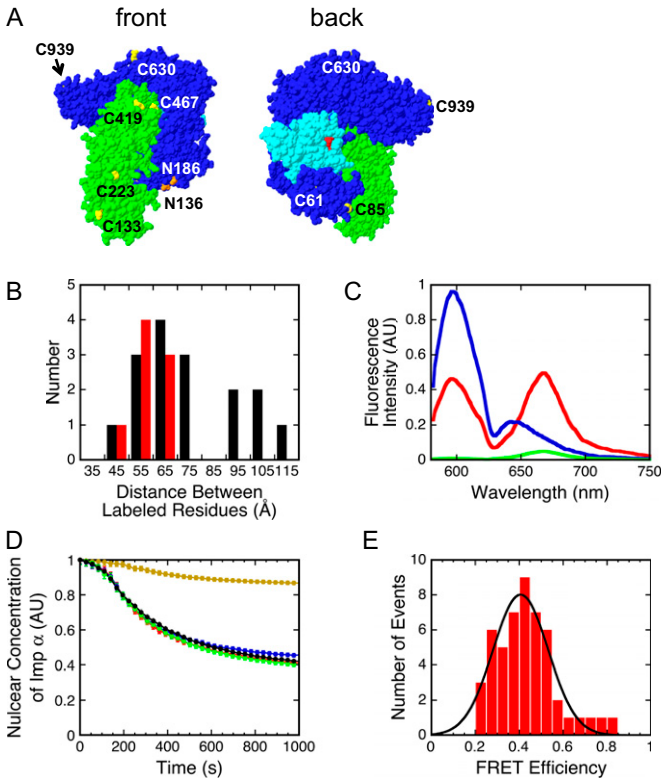

Fig. S1. FRET between Imp-α and mutant CAS (muCAS) and the nuclear export assay. (*A*) Structure of the Kap60p/Cse1p/RanGTP complex [Protein Data Bank (PDB) ID: 1WA5]. Karyopherin α (Kap60p) and Cse1p are the *Saccharomyces cerevisiae* homologs of Imp-α and CAS, respectively. In yellow are the approximate positions of wild-type surface cysteines in human Imp-α (green: C133, C223, C419, and C467) and CAS (blue: C61, C85, C630, and C939) that are expected to be tagged by maleimide dyes. Residues corresponding to N136 and N186 of CAS that were mutated to cysteine to yield muCAS are highlighted in orange. Ran is light blue and GTP is red. C61 is on the concave inner surface of the CAS molecule, near to, but not overlapping, the Ran binding site. (*B*) Histogram of distances between cysteines in Imp-α and CAS. Distances between wild-type cysteine pairs are shown in black. Distances between the N136C and N186C sites on CAS and the Imp-α cysteines are identified in red. The two mutations provide for a number of close contacts, resulting in more efficient FRET. (*C*) FRET between Alexa568-Imp-α (100 nM) and Alexa647-muCAS (500 nM) in the presence of RanGTP (1 μM). Blue, Imp-α alone; red, muCAS + Imp-α + RanGTP; green, muCAS alone. Excitation wavelength = 568 nm. (*D*) Export of Imp-α requires CAS (*Materials and Methods*). Mutation and dye labeling of CAS had no effect on CAS-dependent Imp-α export. Red, wild-type CAS; blue, Alexa568-CAS; green, muCAS; blue, Alexa568-muCAS; brown, no CAS. (*E*) Single-molecule FRET efficiency of coverslip-adsorbed Alexa568-Imp-α/Alexa647-muCAS/RanGTP complexes. For convenience, the FRET efficiency, E, was defined as $E = I_A/(I_A + I_D)$, where I_D and I_A denote the fluorescence emission intensities observed in the donor and acceptor channels, respectively (1). These values were corrected for background noise and the donor emission in the acceptor channel (crosstalk). No detectable acceptor emission was observed in the donor channel. As estimated from a Gaussian fit, the FRET efficiency was 41 ± 13% (n = 50).

1. Ha T (2001) Single-molecule fluorescence resonance energy transfer. *Methods* 25(1):78–86.

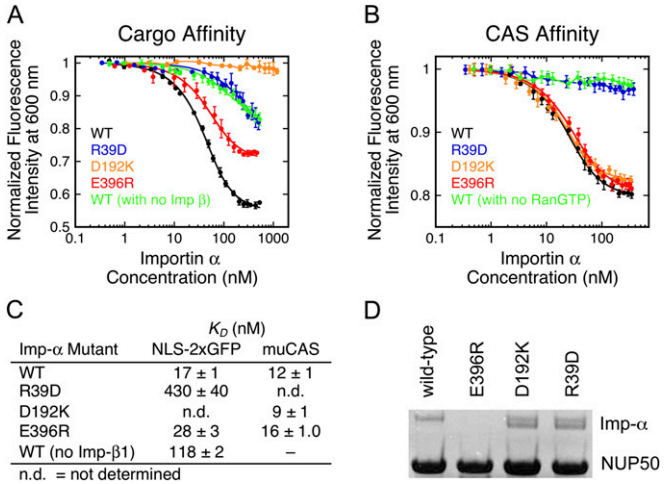

Imp-α Mutant	K_D (nM) NLS-2xGFP	muCAS
WT	17 ± 1	12 ± 1
R39D	430 ± 40	n.d.
D192K	n.d.	9 ± 1
E396R	28 ± 3	16 ± 1.0
WT (no Imp-β1)	118 ± 2	–

n.d. = not determined

Fig. S2. Imp-α mutant affinities for NLS-2xGFP, CAS, and a Nup50 fragment. (*A* and *B*) Imp-α mutant affinity data from titration experiments using FRET. (*A* and *B*) Alexa568-NLS-2xGFP (50 nM) (*A*) and GST-muCAS-Alexa568 (25 nM) (*B*) were titrated with Alexa647-Imp-α and the donor (Alexa568) emission was measured (excitation wavelength = 568 nm; emission wavelength = 600 nm). Imp-β1 (2 μM) and RanGTP (2 μM) were present in *A* and *B*, respectively, unless otherwise indicated. Where possible, the titration data were fitted to a single-site binding model (Eq. **2** and *Materials and Methods*). (*C*) K_D values determined from the data in *A* and *B*. (*D*) Pull-down assays illustrating the binding of the different Imp-α mutants to GST-Nup50 (residues 1–50 of mouse Nup50). The E396R mutant showed negligible binding to the Nup50 fragment, whereas the D192K and R39D mutants display an affinity similar to that of wild-type Imp-α.

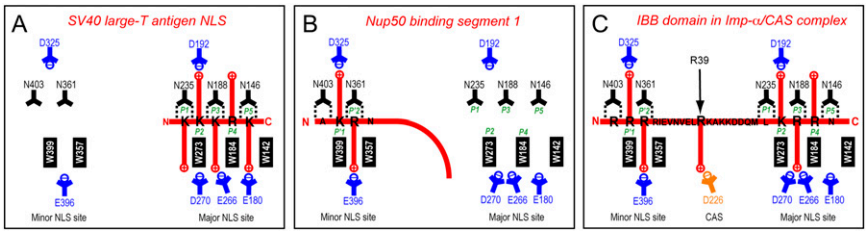

Fig. S3. Schematic illustrations of the interactions affected by the Imp-α mutations. (*A*) Interaction of the SV40 NLS with the major NLS binding site of Imp-α (PDB ID: 1BK6). The D192K mutation disrupts the key salt bridge formed with the P2 lysine residue of the NLS. (*B*) Interaction of Nup50 binding segment 1 with the minor NLS binding site on Imp-α (PDB ID: 2C1M). The E396R mutation disrupts the key salt bridge formed with the P2 arginine residue of Nup50. (*C*) Interaction of the IBB domain with both major and minor NLS binding sites on Imp-α (PDB ID: 1WA5). The R39D mutation disrupts the key salt bridge formed with Asp226 of CAS (orange). Arg39 also interacts with Imp-β (main text).

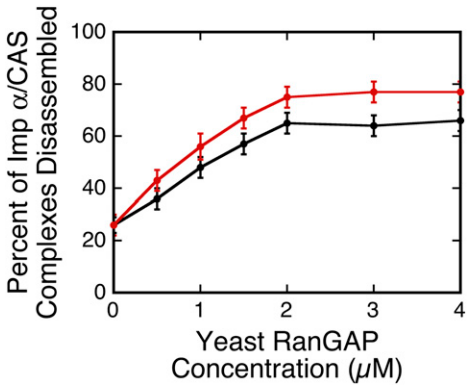

Fig. S4. Effect of yeast RanGAP (rna1p) and mouse Ubc9 on the disassembly of Imp-α/CAS complexes during nuclear export. Shown is the same experiment as in Fig. 8*B*. It is unclear why Ubc9 enhances the effect of yeast RanGAP. One possibility is that Ubc9 can promote binding of yeast RanGAP to mammalian NPCs. Alternatively, Ubc9 could enhance the Ran GTPase activating ability of yeast RanGAP. Black, yeast RanGAP; red, yeast RanGAP + 5 μM Ubc9.

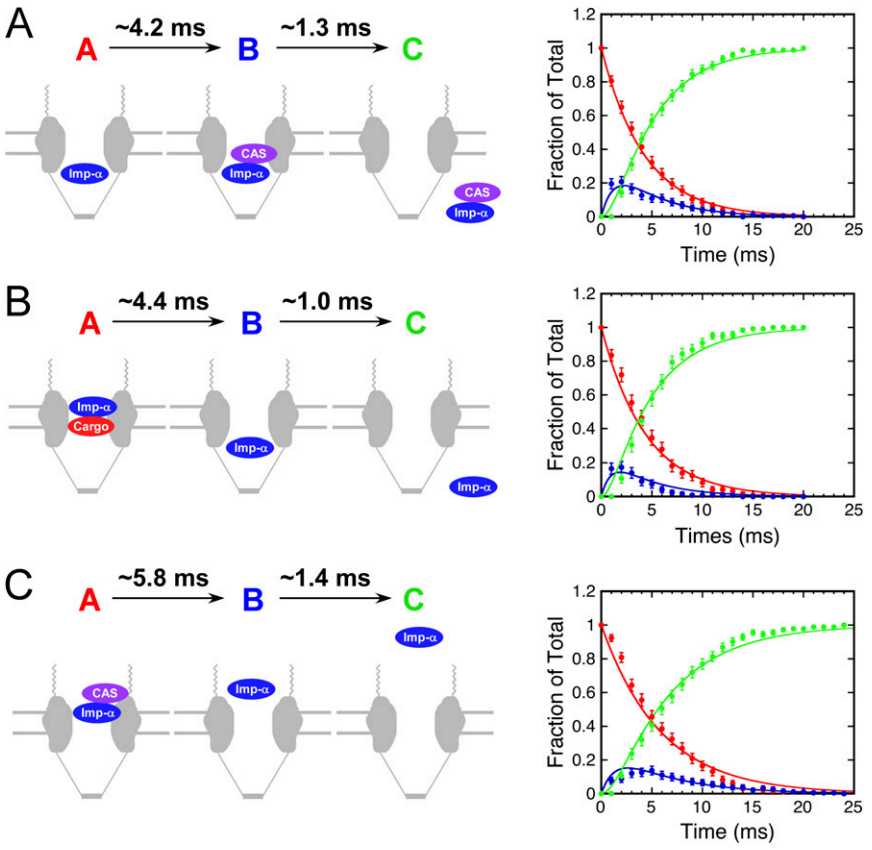

Fig. S5. Kinetics of complex assembly and disassembly. All reactions are modeled as two-step processes, $A \rightarrow B \rightarrow C$. (*A*) Assembly of Imp-α/CAS complexes during nuclear import. Experiment is the same as in Fig. 3*A* ($n = 174$). (*B*) Disassembly of Imp-α/cargo complexes during nuclear import. Experiment is the same as in Fig. 3*D* ($n = 121$). This experiment duplicates the experiment reported earlier (figure S3*B* in ref. 1). The shorter interaction time reported here results from the inclusion of DTT in the transport assay (data not shown). (*C*) Disassembly of Imp-α/CAS complexes during nuclear export. Experiment is the same as in Fig. 6*A*, with Imp-α and CAS only ($n = 182$). See main text for details.

1. Sun C, Yang W, Tu L-C, Musser SM (2008) Single-molecule measurements of importin alpha/cargo complex dissociation at the nuclear pore. *Proc Natl Acad Sci USA* 105(25):8613–8618.

Table S1. Effect of various Imp-α mutations on the Imp-α/CAS complex assembly reaction and the final destination of Imp-α during cargo import

Imp-α mutant	Destination of Imp-α	Imp-α/CAS complex...			*N*
		Did not assemble at the NPC (Imp-α), %	Assembled at the NPC (Imp-α/CAS), %	Disassembled before leaving the NPC (Imp-α), %	
WT Imp-α	Cytoplasm	21 ± 2	17 ± 2	9 ± 2	287
	Nucleoplasm	11 ± 2	36 ± 3	6 ± 1	
D192K	Cytoplasm	35 ± 3	22 ± 3	0	214
	Nucleoplasm	27 ± 3	16 ± 3	0	
E396R	Cytoplasm	51 ± 3	5 ± 1	0	225
	Nucleoplasm	36 ± 3	8 ± 2	0	
R39D	Cytoplasm	50 ± 3	3 ± 1	0	207
	Nucleoplasm	43 ± 3	2 ± 1	2 ± 1	

Numerical data for Figs. 4 and 5. All reactions included 0.1 nM of the Alexa568-labeled Imp-α mutant and 250 nM Alexa647-muCAS.

Table S2. Effect of RanBP1 concentration on the disassembly of Imp-α/CAS complexes and the final destination of Imp-α during CAS-dependent export

RanBP1, μM	Destination of Imp-α	Imp-α/CAS complex... Remained intact at the NPC (Imp-α/CAS), %	Imp-α/CAS complex... Disassembled at the NPC (Imp-α), %	Disassembly efficiency, %	*N*
0	Cytoplasm	51 ± 4	14 ± 3	20 ± 3	168
	Nucleoplasm	29 ± 4	6 ± 2		
+ 3 μM RanGAP					
0	Cytoplasm	41 ± 5	29 ± 4	40 ± 5	112
	Nucleoplasm	19 ± 4	11 ± 3		
0.5	Cytoplasm	36 ± 4	36 ± 4	46 ± 4	126
	Nucleoplasm	18 ± 3	10 ± 3		
1	Cytoplasm	32 ± 4	42 ± 4	55 ± 4	132
	Nucleoplasm	13 ± 3	13 ± 3		
1.5	Cytoplasm	29 ± 4	45 ± 5	59 ± 5	108
	Nucleoplasm	12 ± 3	14 ± 3		
2	Cytoplasm	25 ± 4	51 ± 4	65 ± 4	137
	Nucleoplasm	10 ± 3	14 ± 3		
3	Cytoplasm	23 ± 4	47 ± 4	64 ± 4	128
	Nucleoplasm	13 ± 3	17 ± 3		
4	Cytoplasm	20 ± 3	49 ± 4	62 ± 4	140
	Nucleoplasm	18 ± 3	13 ± 3		
+ 3 μM SUMO1-RanGAP					
0	Cytoplasm	35 ± 4	32 ± 4	45 ± 4	127
	Nucleoplasm	20 ± 4	13 ± 3		
0.5	Cytoplasm	32 ± 4	38 ± 4	52 ± 4	135
	Nucleoplasm	16 ± 3	14 ± 3		
1	Cytoplasm	29 ± 4	44 ± 5	58 ± 5	117
	Nucleoplasm	13 ± 3	14 ± 3		
1.5	Cytoplasm	25 ± 4	48 ± 4	63 ± 4	125
	Nucleoplasm	12 ± 3	15 ± 3		
2	Cytoplasm	18 ± 3	53 ± 4	71 ± 4	134
	Nucleoplasm	11 ± 3	18 ± 3		
3	Cytoplasm	20 ± 4	50 ± 4	66 ± 4	127
	Nucleoplasm	14 ± 3	16 ± 3		
4	Cytoplasm	19 ± 3	54 ± 4	69 ± 4	130
	Nucleoplasm	12 ± 3	15 ± 3		
+ 3 μM SUMO1-RanGAP and 5 μM Ubc9					
0	Cytoplasm	33 ± 4	38 ± 5	49 ± 5	116
	Nucleoplasm	18 ± 4	11 ± 3		
0.5	Cytoplasm	29 ± 4	44 ± 4	56 ± 4	126
	Nucleoplasm	15 ± 3	12 ± 3		
1	Cytoplasm	25 ± 4	45 ± 5	63 ± 5	104
	Nucleoplasm	12 ± 3	18 ± 4		
1.5	Cytoplasm	21 ± 4	53 ± 5	69 ± 4	122
	Nucleoplasm	10 ± 3	16 ± 3		
2	Cytoplasm	19 ± 3	60 ± 4	78 ± 4	136
	Nucleoplasm	3 ± 1	18 ± 3		
3	Cytoplasm	18 ± 3	59 ± 4	77 ± 4	128
	Nucleoplasm	5 ± 2	18 ± 3		
4	Cytoplasm	15 ± 3	63 ± 4	79 ± 4	116
	Nucleoplasm	6 ± 2	16 ± 3		

Numerical data for Figs. 7 and 8. All reactions included 0.1 nM Alexa568-Imp-α and 250 nM Alexa647-muCAS. RanBP1, Ran binding protein 1.

Table S3. Effects of RanGAP and SUMO1-RanGAP concentration on the disassembly of Imp-α/CAS complexes and the final destination of Imp-α during CAS-dependent export in the presence of RanBP1

Conditions	Destination of Imp-α	Imp-α/CAS complex... Remained intact at the NPC (Imp-α/CAS), %	Imp-α/CAS complex... Disassembled at the NPC (Imp-α), %	Disassembly efficiency	*N*
RanGAP, μM					
0	Cytoplasm	43 ± 4	21 ± 4	26 ± 4	123
	Nucleoplasm	31 ± 4	5 ± 2		
0.5	Cytoplasm	40 ± 4	25 ± 4	36 ± 4	142
	Nucleoplasm	24 ± 4	11 ± 3		
1	Cytoplasm	32 ± 4	31 ± 4	48 ± 4	137
	Nucleoplasm	20 ± 3	17 ± 3		
1.5	Cytoplasm	25 ± 4	41 ± 4	57 ± 4	151
	Nucleoplasm	18 ± 3	16 ± 3		
2	Cytoplasm	21 ± 4	45 ± 4	65 ± 4	132
	Nucleoplasm	14 ± 3	20 ± 3		
3	Cytoplasm	23 ± 4	47 ± 4	64 ± 4	128
	Nucleoplasm	13 ± 3	17 ± 3		
4	Cytoplasm	25 ± 4	51 ± 4	66 ± 4	139
	Nucleoplasm	9 ± 2	15 ± 3		
SUMO1-RanGAP, μM					
0	Cytoplasm	43 ± 4	21 ± 4	26 ± 4	123
	Nucleoplasm	31 ± 4	5 ± 2		
0.5	Cytoplasm	41 ± 4	24 ± 4	38 ± 4	148
	Nucleoplasm	21 ± 3	14 ± 3		
1	Cytoplasm	32 ± 4	39 ± 4	52 ± 5	122
	Nucleoplasm	16 ± 3	13 ± 3		
1.5	Cytoplasm	29 ± 4	42 ± 4	60 ± 4	130
	Nucleoplasm	11 ± 3	18 ± 3		
2	Cytoplasm	18 ± 4	46 ± 5	68 ± 4	116
	Nucleoplasm	14 ± 3	22 ± 4		
3	Cytoplasm	20 ± 4	50 ± 4	66 ± 4	127
	Nucleoplasm	14 ± 3	16 ± 3		
4	Cytoplasm	18 ± 3	53 ± 4	69 ± 4	141
	Nucleoplasm	13 ± 3	16 ± 3		
SUMO1-RanGAP (μM) and 5 μM Ubc9					
0	Cytoplasm	43 ± 4	21 ± 4	26 ± 4	123
	Nucleoplasm	31 ± 4	5 ± 2		
0.5	Cytoplasm	39 ± 4	27 ± 4	43 ± 5	120
	Nucleoplasm	18 ± 4	16 ± 3		
1	Cytoplasm	32 ± 4	43 ± 5	56 ± 5	118
	Nucleoplasm	12 ± 3	13 ± 3		
1.5	Cytoplasm	26 ± 4	45 ± 4	67 ± 4	133
	Nucleoplasm	18 ± 3	21 ± 4		
2	Cytoplasm	14 ± 3	52 ± 4	75 ± 4	147
	Nucleoplasm	11 ± 3	23 ± 3		
3	Cytoplasm	18 ± 3	59 ± 4	77 ± 4	128
	Nucleoplasm	5 ± 2	18 ± 3		
4	Cytoplasm	13 ± 3	60 ± 4	77 ± 4	136
	Nucleoplasm	10 ± 3	17 ± 3		

Numerical data for Figs. 7 and 8. All reactions included 0.1 nM Alexa568-Imp-α, 250 nM Alexa647-muCAS, and 3 μM RanBP1.

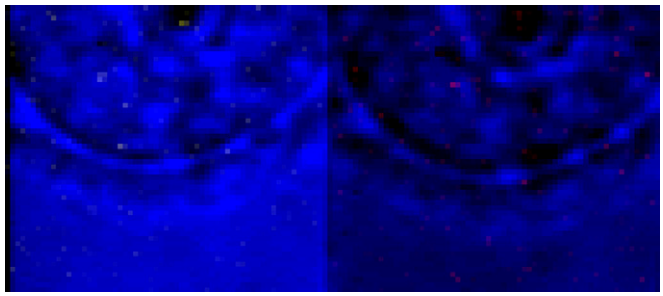

Movie S1. Import event shown in Fig. 1 *A–C*. Playback speed is two frames per second. Blue, bright-field image; yellow, Alexa568-Imp-α (donor) fluorescence intensity; red, Alexa647-muCAS (acceptor) fluorescence intensity. Pixel size is ∼240 nm and each frame was acquired in 1 ms.

Movie S1

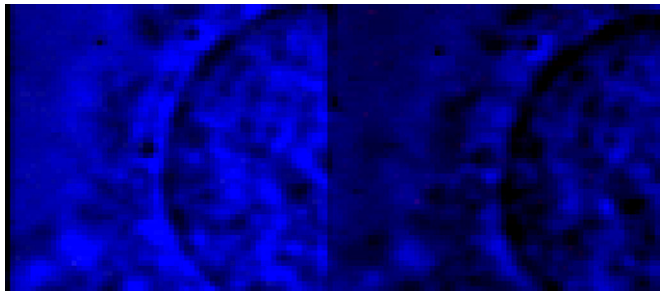

Movie S2. Export event shown in Fig. 1 *D–F*. Playback speed is two frames per second. Blue, bright-field image; yellow, Alexa568-Imp-α (donor) fluorescence intensity; red, Alexa647-muCAS (acceptor) fluorescence intensity. Pixel size is ∼240 nm and each frame was acquired in 1 ms.

Movie S2

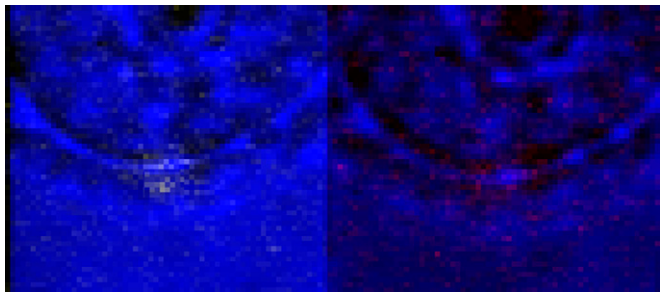

Movie S3. Dissociation of an Imp-α/CAS complex after 1 ms during nuclear import. One of the events in Fig. 3*B* is shown. Same conditions as in Movie S1 are shown. Pixel size is ∼240 nm and each frame was acquired in 1 ms.

Movie S3

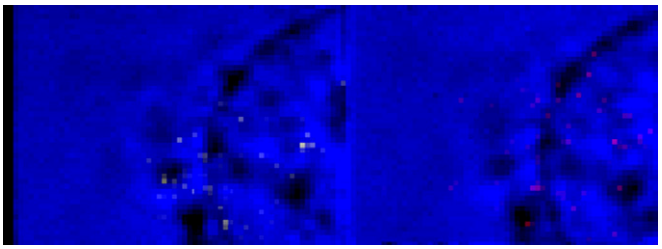

Movie S4. smFRET between NLS-2xGFP and CAS shown in Fig. 3*E*. Playback speed is one frame per second. Blue, bright-field image; yellow, Alexa568-NLS-2xGF(4C) (donor) fluorescence intensity; red, Alexa647-muCAS (acceptor) fluorescence intensity. Pixel size is ~240 nm and each frame was acquired in 1 ms.

Movie S4